



Fracture and creep of glass–ceramic solid oxide fuel cell sealant materials



J. Malzbender*, Y. Zhao, T. Beck

Forschungszentrum Jülich GmbH, IEK-2, 52425 Jülich, Germany

HIGHLIGHTS

- Partially crystallized sealants showed thickness dependent fracture stress.
- Measured fracture stress is affected by residual stress.
- Creep rate dependent on crystallization stage.
- Partially crystallized sealant shows enhanced creep and reduced strength.

ARTICLE INFO

Article history:

Received 20 June 2013

Received in revised form

31 July 2013

Accepted 3 August 2013

Available online 13 August 2013

Keywords:

Solid oxide fuel cells

Sealant

Mechanical properties

Creep

Glass–ceramic

ABSTRACT

The reliable operation of solid oxide fuel cell stacks depends strongly on the structural integrity of the sealing materials. In this respect, failure and deformation are aspects which need to be assessed in particular for glass–ceramic sealant materials. Bending tests and compressive tests were carried at room temperature and typical stack operation temperature for sintered bars and stack similar head-to-head joined glass–ceramic sealants specimens with different degree of crystallization and annealed temperature. The sealant material was screen printed onto the steel. Fracture stresses and creep data are reported. The results reveal a thickness dependent fracture stress and a decrease of the fracture stress for the partially crystallized sealant at operation relevant temperatures that can be associated with the residual stress state and viscous deformation of the material, respectively. A stable thickness independent fracture stress was obtained for the fully crystallized sealant. Fractographic based analysis gave insight into the failure origin.

© 2013 Elsevier B.V. All rights reserved.

1. Introduction

Solid oxide fuel cells convert chemical energy into electricity and can reach very high efficiencies as compared to conventional thermal energy conversion systems [1,2]. The Forschungszentrum Jülich has been working in the area of solid oxide fuel cell for more than 15 years, covering aspects from basic materials research to systems design [2]. The cells in the Jülich design are fixed and sealed in a frame between interconnected plates to form a repeating unit and finally a stack. The bonding between the ceramic cell and the metallic interconnect in the stationary design is currently achieved by glass–ceramic sealants [3], which appear to fulfill the requirements with respect to gas tightness, high temperature stability and electrical insulation [4]. However, failure and deformation are aspects that need to be assessed to warrant the

reliability of SOFC stacks and system [5]. BaO–CaO–SiO₂ materials are used as sealants [3,5] in Jülich. In order to reduce residual stresses, the sealants are tailored to match the thermal expansion coefficients of the adjacent materials, cell (anode substrate) and interconnect, which in turn are chosen to match each other closely. Another most important criterion is the glass transition temperature T_g , above which the materials change from brittle to ductile behavior. However, in addition to viscous stress relaxation the occurrence of structural instabilities might be expected above T_g . The current work concentrates on the mechanical characterization of two glass–ceramic sealants. One ceramic filler particle reinforced sealant with a rather low level of crystallization (abbreviated H, 80% glassy phase) and one without reinforcement which is almost fully crystallized (B, ~10% glassy phase) [6–8].

The current study aims to investigate the effect of the sealant layer thickness on the materials' strength and elevated temperature deformation behavior and how it is influenced by aging/crystallization effects at operation temperatures. The main focus of the work is placed to the sealing area responsible for outer leakages,

* Corresponding author.

E-mail address: j.malzbender@fz-juelich.de (J. Malzbender).

where only steel parts are joined. At operation relevant temperatures, long-term failure may occur due to viscous damage. Hence, compressive tests were carried out to assess relevant creep parameters. Furthermore, the results are correlated with microstructural observations.

2. Experimental

The partially crystallized glass–ceramic (H) is based on a glass matrix of the BaO–CaO–SiO₂ ternary system with small amounts of Al₂O₃, B₂O₃, V₂O₅, and ZnO [3]. The raw materials were obtained from Merck KGaA, Darmstadt (purity grade > 99%). Each individual batch was processed by mixing an appropriate mole fraction of oxide ingredients and melting at 1480 °C in a platinum crucible in an induction furnace [3]. For a better homogenization, the melting procedure was carried out twice. For subsequent powder preparation, the frits were acetone wet-milled in an agate ball mill to a median particle size of 10–13 µm, dried and sieved. The chemical composition was analyzed by inductively coupled plasma optical emission spectroscopy (ICP-OES) yielding BaO – 48.2, SiO₂ – 29.8, and CaO – 6.1 wt.% with minor additions of Al₂O₃, B₂O₃, V₂O₅, and ZnO. A conventional sintering process was carried out to obtain sintered rods; powders were mixed with YSZ particles (sizes 1–40 µm) and pressed and sintered on a wavelike curved platinum foil at 850 °C for 10 h and then cooled down to room temperature (RT). Heating and cooling rates were 5 K min⁻¹.

The almost fully crystallized glass–ceramic (B) is also based on the BaO–CaO–SiO₂ system, however, with addition of only Al₂O₃. The processing routine corresponded to that of the H series [3]. Analysis by ICP-OES yielded BaO – 36.7, SiO₂ – 46.8, and CaO – 15.8 wt.%, with minor additions of Al₂O₃. The powder was pressed and sintered at 950 °C for 10 h (heating, cooling rate 5 K min⁻¹).

Details on the preparation of sintered bars are given in Refs. [7,8]. Head-to-head joined specimens were prepared using an in-house developed sealing jig [7], where similar as in SOFC stacks, Crofer22APU was used as steel, with a surface preparation equivalent to the stack application. The sealant was deposited by screen printing. Specimens' dimensions were 52 mm × 6 mm × 4 mm, sealant thickness varied between ~50 and ~400 µm (Fig. 1). The analysis of the fracture stresses of the head-to-head joined specimens followed ASTM C1161. The viscous deformation was investigated for bending bars and head-to-head joined specimens. Details on the subcritical crack growth analysis and strength–probability–time diagram construction can be found in Ref. [9] on the strength test in Refs. [7,10,11], on the microstructural/fractographic analysis are given in Refs. [12,13] and on the creep tests in Refs. [14,15].

Crystalline phases of the glass ceramics before and after 500 h annealing were examined by X-ray diffraction at ambient temperature using a step scan procedure (0.02°/2θ step, count time 5 s) with a crystal monochromator employing Cu-Kα radiation. The

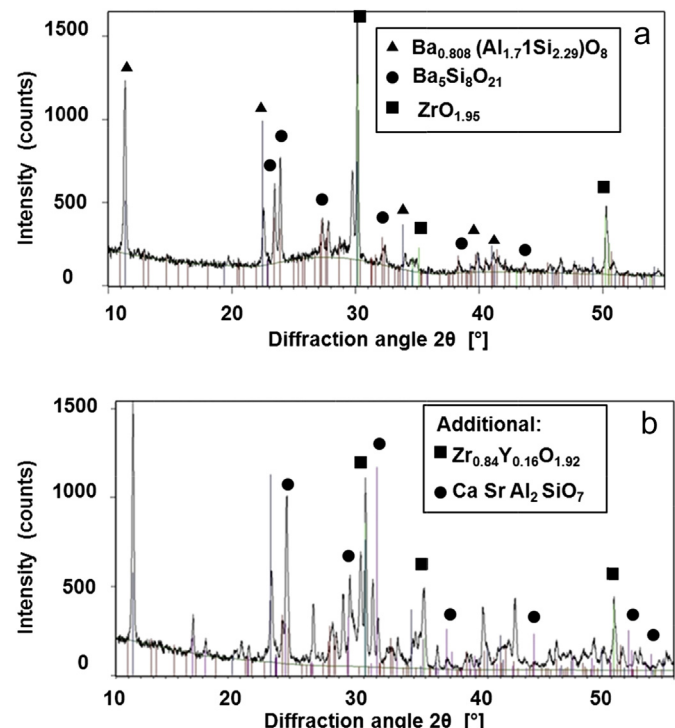


Fig. 2. XRD patterns of the sealant H–P, (a) sintered state and (b) annealed state.

microstructure of the polished cross-sections of the non-aged and aged glass ceramics were examined using a Zeiss Ultra 55 scanning electron microscope (SEM).

3. Results and discussion

X-ray diffraction patterns have been obtained for H–P and B specimen bars. Fig. 2 shows the XRD patterns for the non-aged and aged H–P material (annealed at 800 °C for 500 h). Only few phase peaks were found in the non-aged H–P material (~10% crystalline phases). The high background (green line (in the web version only)) with a raise of the baseline between 20 and 35° is an indication of a high content of amorphous phase. However, the number of phase peaks increases significantly for the aged H–P material in comparison to the non-aged state indicating existence of different crystalline phases in this material. Compared with the non-aged H–P material, the new crystalline phases Zr_{0.84}Y_{0.16}O_{1.92} and CaSrAl₂SiO₇ appeared after aging in addition to the Ba_{0.808}(Al_{1.7}Si_{2.29})O₈, Ba₅Si₈O₂₁ phases, which existed already in the non-aged material. Note, microstructural images after different annealing and stack operation times can also be found in Ref. [16].

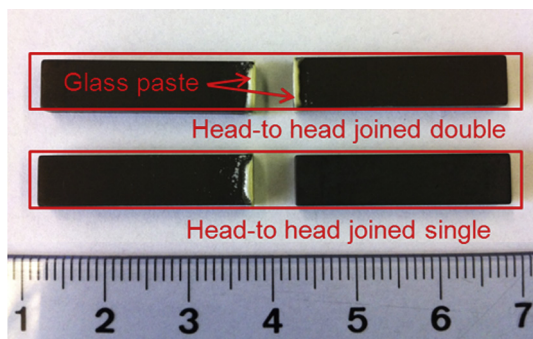


Fig. 1. Double and single layer head-to-head joined specimens.

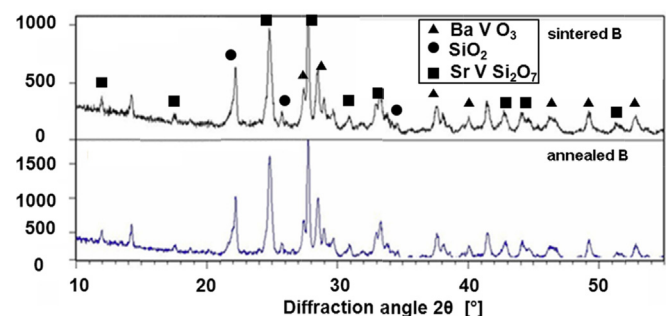


Fig. 3. XRD patterns of the as joined sealant B.

Table 1

Fracture stresses of material H–P and B for sandwich specimens.

Material		Av. fracture stress, MPa	Characteristic strength, MPa	Weibull modulus	Sealant thickness, μm
H–P	Double	22 \pm 2	23	9	350 \pm 60
	Single	34 \pm 6	36	6	153 \pm 45
B	Double	25 \pm 2	26	15	319 \pm 60
	Single	25 \pm 5	27	5	173 \pm 54

For material B, the XRD spectra in Fig. 3 reveal the same pattern for the non-aged and aged (annealed at 800 °C for 500 h) specimens. No new crystalline phases form after 500 h annealing. This implies that the material is in a stable crystallization state after sintering at 950 °C for 10 h. The volume fraction of crystalline phases is basically unchanged after an additional annealing for 500 h at 800 °C verifying that the main crystallization happens during the initial sealing step for material B. Note, XRD spectra in Refs. [6,7] correspond only to material H–P. A number of specimens have been analyzed microstructurally with respect to pores and crystallization morphology. Overall there was no systematic local enhancement of the distribution with respect to center or specimens edge.

The assessment of the mechanical parameters was based on four-point bending tests of head-to-head joined H–P and B type specimens in a more stack typical geometry than in the previous tests which concentrated on sintered bars [7]. To get close to the

real stack like sealant thickness, two methods to enhance the thickness were tested, multiple screen printing and printing on both steel substrates. This along with an adjustment of the joining jig yielded for a deposition on one steel specimen an average thickness of around 150 μm and 300 μm for the deposition on both substrates. The subsequently determined fracture stresses are given in Table 1. Weibull statistics was applied to analyze the fracture stresses. The two parameter Weibull distribution of fracture stresses of materials H–P and B are shown in Fig. 4. The characteristic strengths are given in Table 1.

The tested volume of the glass–ceramics correspond approximately to the cross-sectional area of the bar (4 mm \times 6 mm) times the individual layer thickness of the particular specimen. The number of specimens for the H–P single and double was ten each, for the B single and double eight each, hence the estimated Weibull moduli are only a rough guideline since, first, an accurate determination of the Weibull modulus requires at least 30 specimens and second, especially for material H–P, the fracture stress depends on the layer thickness as will be discussed below and hence, it would only be possible to describe the data accurately by a Weibull statistics if all data are obtained for one particular layer thickness.

The average fracture stress of the single side deposited H–P is higher than for the double side deposited H–P, hence the head-to-head joined H–P specimens clearly reveal an influence of the thickness (Fig. 5). This suggests that the compressive residual stress generated during cooling to RT enhances the fracture stress, since the thermal expansion coefficient of this sealant is lower than that

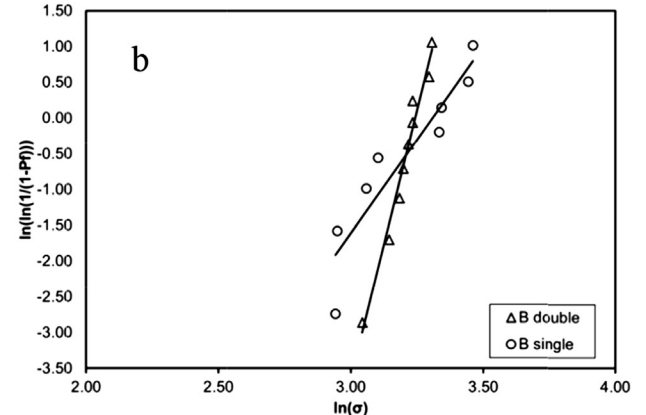
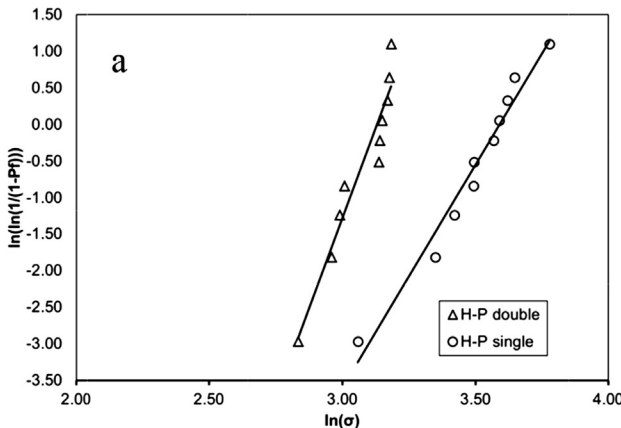


Fig. 4. Weibull representation of the fracture stresses of material (a) H–P and (b) B.

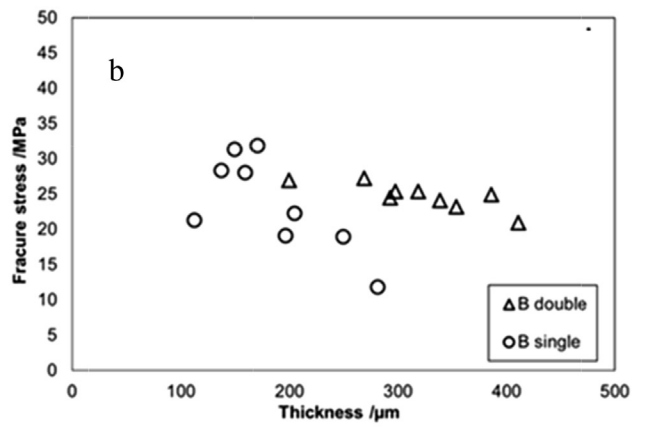
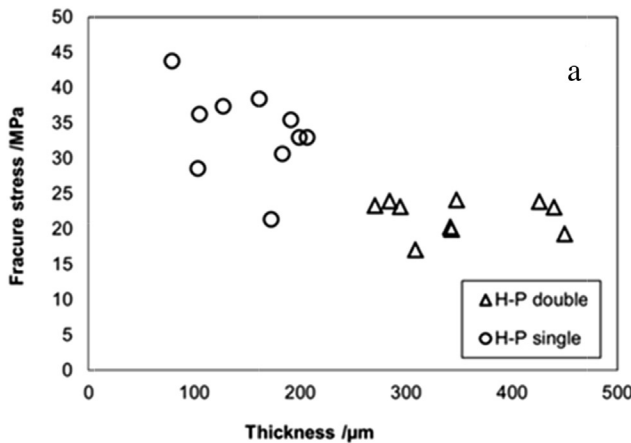


Fig. 5. Fracture stresses as a function of thickness for materials (a) H–P and (b) B.

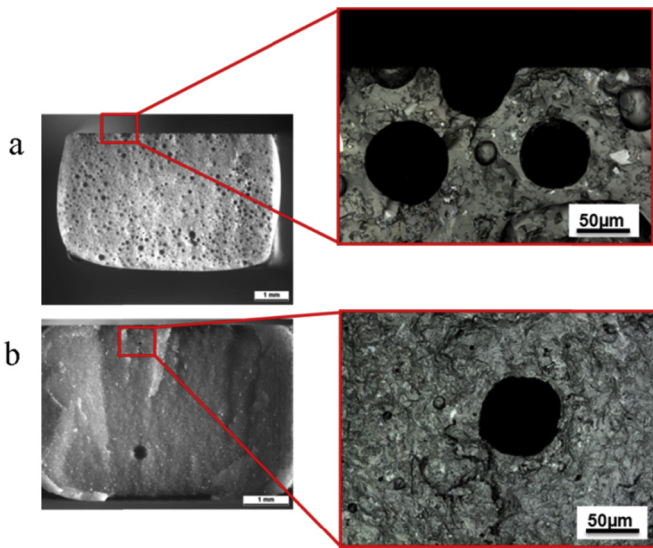


Fig. 6. Fracture surfaces of head joined (a) H-P and (b) B specimens.

of the used steel substrates [8]. The thinner the sealant layer, the higher is the residual stress. Contrary to this, the fracture stresses of material B, which has a thermal expansion coefficient that is closer to that of the steel [8], did not show a dependency on specimens' thickness within the limit of experimental uncertainty (Fig. 5).

Fractographic investigations were carried out to determine failure mode and origin. The fracture surface and fracture origin of both, material H-P and B have been assessed by stereo and confocal microscopy (see Fig. 6). For all head-to-head joined specimens failure occurred through the sealant material, no indication of interfacial failure could be observed. The fracture origin of head-to-

Table 2
Fracture stresses of sintered and annealed H-P sandwich specimens.

Material	Av. fracture stress, MPa	Sealant thickness, μm
H-P As sintered	36 ± 1	71 ± 8
Annealed 800 °C/500 h	47 ± 3	104 ± 3
Annealed 850 °C/500 h	47 ± 4	95 ± 6

head joined H-P specimens appears to be related to open pores in the tensile surface. Compared to the head-to-head joined material H-P specimens, head-to-head joined B sealant has a much finer structure (Fig. 6). However, in the example a big pore is visible near the tensile surface and even a bigger one close to the compressive surface. Failure appears to be related to pores with sizes of up to ~100 μm [7].

Based on a Weibull approach it might be suggested that the strength should decrease for larger components, however, previous investigations for bar type specimens yielded higher fracture stresses than for the head-to-head joined specimens, even though the effective volume of the specimens was larger. For both sealants, the reasons are the differences in pore sizes and overall porosity of the head-to-head joined material (Fig. 7) associated with the evaporation of binder from the glass paste during sintering. Large pores were only observed in the fracture surface of the head-joined B specimens (Fig. 7), not for B type bars (Fig. 6).

Head-to-head joined H-P specimens (Table 2) have been annealed for 500 h at 800 °C and 850 °C, respectively, to study the effect of the crystallization, considering a typical stack operation temperature and the effect of additional annealing at the typical sealing temperature, respectively. The fracture stresses have been determined for the non-annealed and annealed head-to-head joined H-P specimens from the same batch to avoid that the results are biased by the individual specimens' thickness (Table 2). Material B was not tested since it was verified previously [6] that

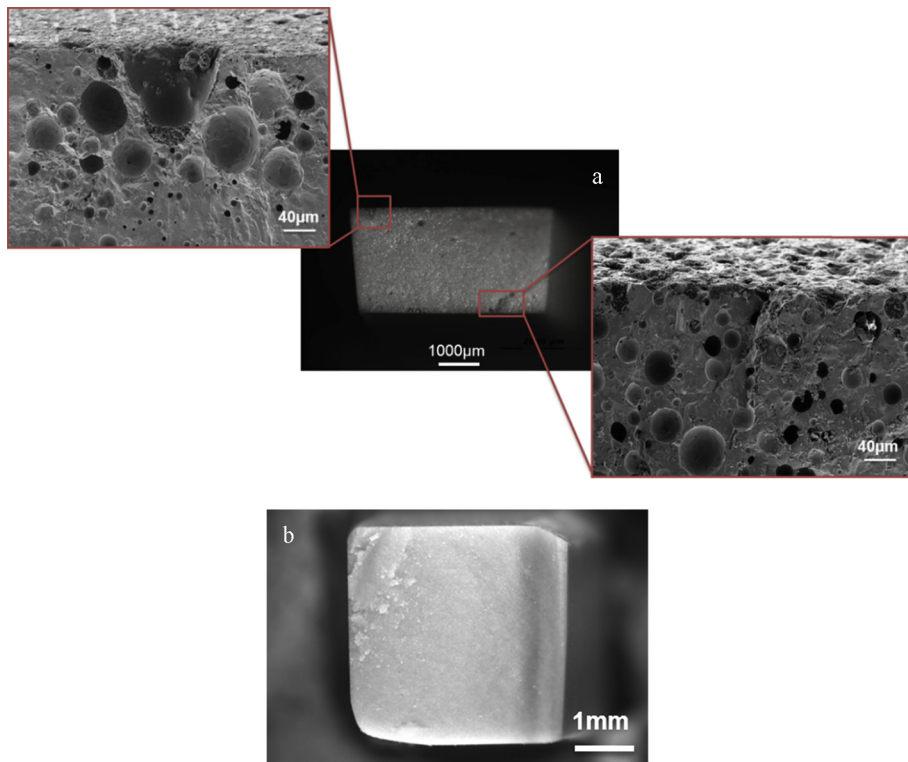


Fig. 7. Fracture surface after bending test of a (a) H-P type bar and (b) B type bar.

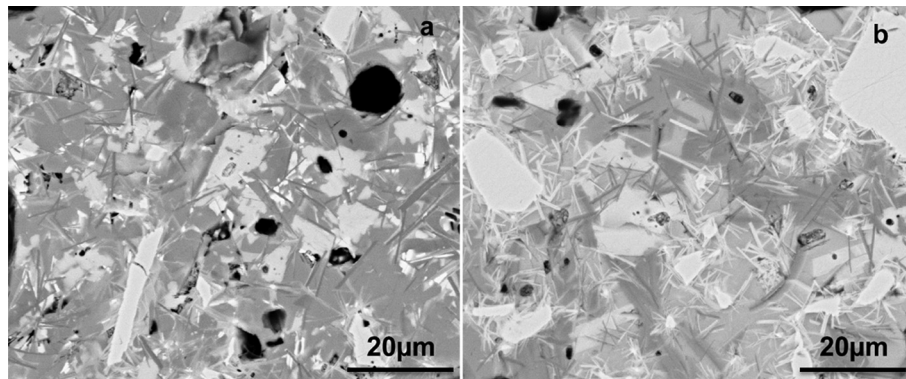


Fig. 8. SEM images annealed H-P at (a) 800 °C and (b) 850 °C, initial state see Ref. [6].

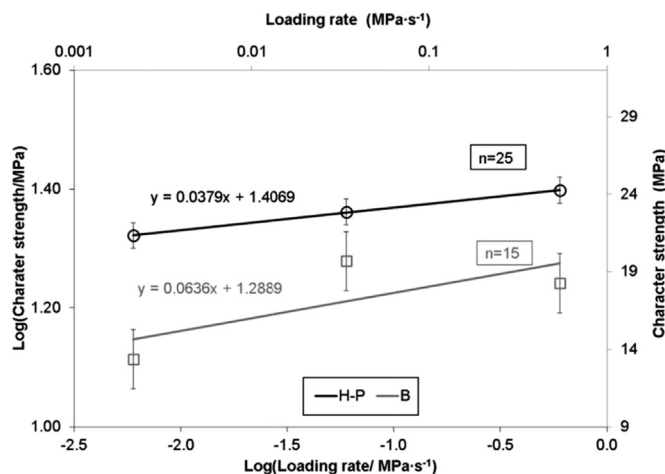


Fig. 9. Characteristic strength as a function of loading rate for materials H-P and B.

the mechanical properties of this material are not influenced by annealing effects; the material is almost fully crystallized and the crystallization state is stable.

The tests revealed that the fracture stresses of the H-P material increases in both cases by 30% due to the further crystallization (Fig. 8). Especially specimens after 500 h at 850 °C contained more white needle like crystallized structures (~30% volume fraction).

Considering the high porosity of the H-P material, again open pores in the tensile loaded surface probably led to the failure. All specimens revealed a fracture path in the middle of the glass ceramic layers.

The sintered H-P specimens revealed similar fracture stresses below 700 °C, and a strong decrease around 800 °C (to ~1 MPa). The fracture stress of the annealed H-P material (with larger degree of crystallization ~30% compared with sintered H-P ~10%) was stable even at high temperature. The almost fully crystallized head-to-head joined sealant B showed also similar fracture stresses at 800 °C as at room temperature. Hence crystallization stabilizes the mechanical properties at elevated temperatures.

The subcritical crack growth sensitivity of materials H-P and B in air has been analyzed in the head-to-head joined geometry based on the fracture stress values measured at the loading rates 0.006 MPa s⁻¹, 0.06 MPa s⁻¹ and 0.6 MPa s⁻¹ (ten specimens each with one particular thickness). A comparison of the behavior of the materials is given in Fig. 9. The data were mathematically described as outlined in Ref. [9]. The derived SCG parameters for sealant B are $n \sim (15 \pm 7)$ and $D \sim (20 \pm 1)$. For H-P specimens the values were $n \sim (25 \pm 2)$ and $D \sim (25 \pm 0.6)$, hence material B appears to be more affected by crack growth at subcritical stress. The n parameter compares well with data for glass (15–30) [9].

The relationship between strength, failure probability and time was used for lifetime prediction of B and H-P materials (see Ref. [12]). Based on a strength–probability–time (SPT) diagram, the design stress for an acceptable failure probability at a given lifetime

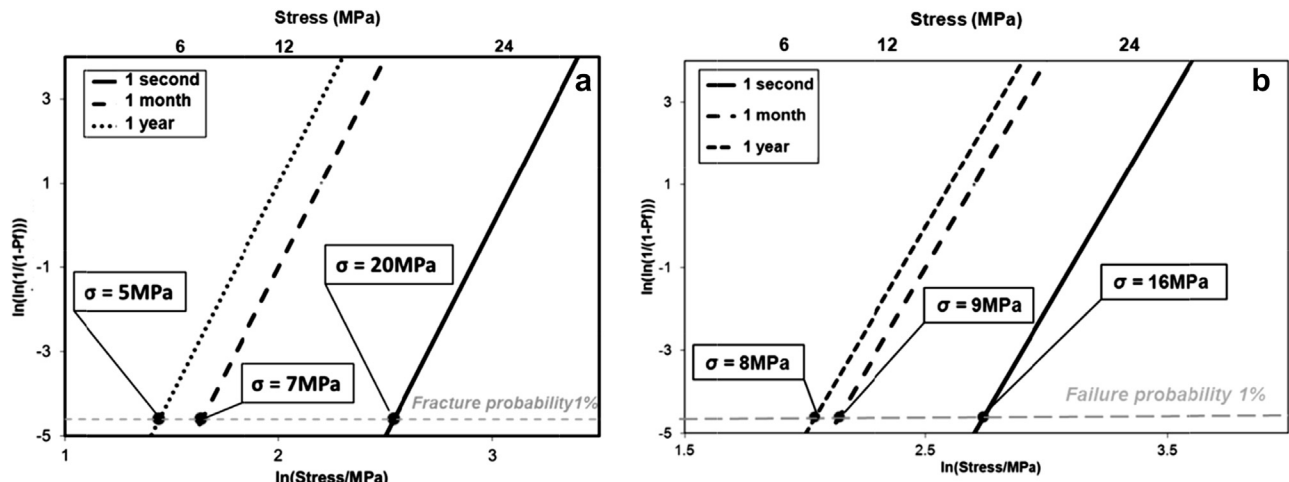


Fig. 10. Strength–probability–time plot for materials (a) B and (b) H-P.

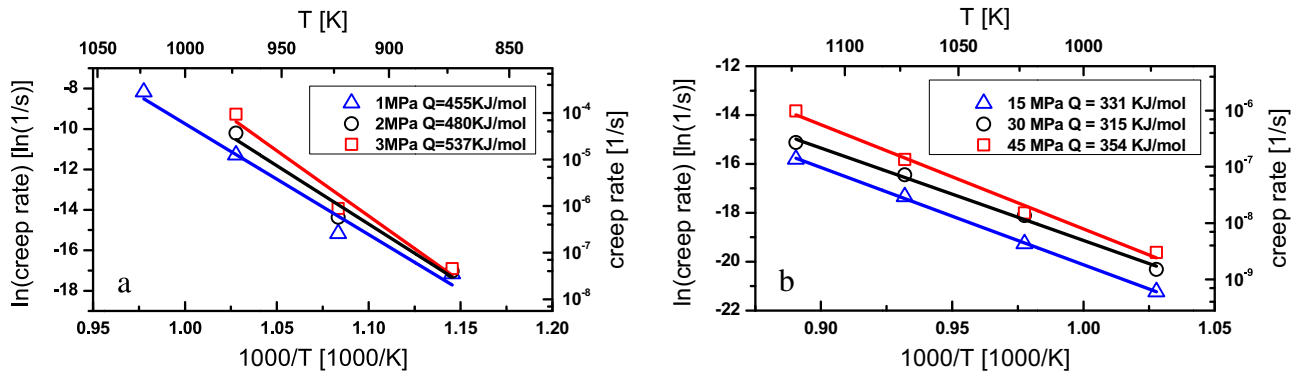


Fig. 11. Equivalent strain rate as a function of $1000/T$ for sintered H-P bars (upper graph) and annealed H-P bars (at $800\text{ }^{\circ}\text{C}$ for 500 h) (lower graph).

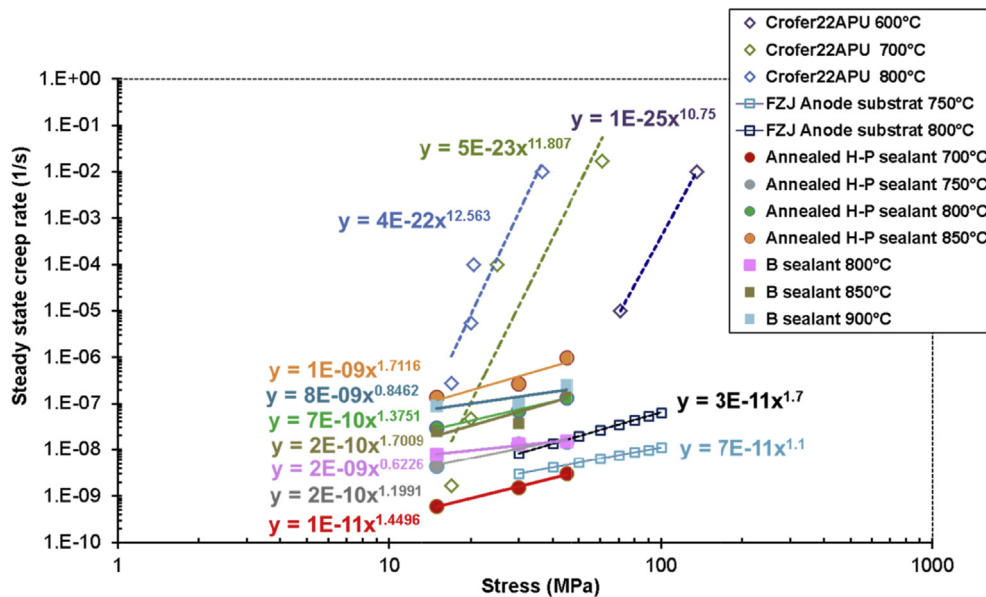


Fig. 12. Norton plots for Crofer22APU [20], anode substrate [21] and sealant H-P and B at different temperatures.

can be estimated. For material B and H-P at room temperature (Fig. 10), the stresses should be not higher than $\sim 5\text{--}8\text{ MPa}$ for a 1% failure probability and one year lifetime. Again this plot should only serve as a guideline due to the obvious uncertainties in the Weibull moduli discussed above.

Compressive tests have been carried out to assess the creep behavior and the results were described by a standard creep equation (see Ref. [14]) in order to obtain the creep parameters (see Fig. 11). The activation energies for creep of sintered and annealed H-P bars are determined from the slope of the trend line of the natural logarithm of strain rate versus the reciprocal temperature. The activation energy of the annealed bar is around $300\text{--}350\text{ kJ mol}^{-1}$ and does not change with the applied stress. The stress exponent n has been determined from a plot of the natural logarithm of strain rate versus the natural logarithm of the stress. The stress exponent for the annealed H-P specimens and B specimens is about 1 within the limits of uncertainty independent of the temperature, which indicates Newtonian viscous flow [17]. The stress exponents of sintered H-P bars increased from 0.2 (± 0.03) to 1.8 (± 0.2), which is considered to be a result of a mechanism change from diffusional to viscous creep. The activation energies for as sintered bars H-P obtained for lower stresses (1 MPa, 2 MPa, 3 MPa)

yielded higher activation energy values (above 400 kJ mol^{-1}) than for annealed bars H-P and sintered bars B. The higher activation energy indicates a thermally activated crystallization kinetics for the sintered bars [18]. This is similar to values reported [19] for magnesia–silica (450 kJ mol^{-1}) and alkali–silica glass (550 kJ mol^{-1}). Furthermore, also the Ba–B–Si–Al–O glass system revealed similar activation energies ($442\text{--}445\text{ kJ mol}^{-1}$) and stress exponents (~ 1) for similar temperatures [20]. The specimens after creep testing showed no significant microstructural changes.

The creep strain rates of annealed H-P and B bar specimens have been plotted as a function of the applied stress for different temperatures in Fig. 12. For stresses around 10 MPa the deformation behavior of the sealant will have a stronger effect than the typical interconnect material steel Crofer22APU [21] and the anode substrate [22].

4. Conclusions

Due to the high requirements on the reliability of solid oxide fuel cell stacks and hence also on the used glass–ceramic sealant, the mechanical properties need to receive considerable attention. In this comparative approach the selected mechanical aspects of a

partial and a fully crystallized material, H–P and B, respectively, were characterized. Failure and deformation are assessed at room temperature and relevant stack operation temperature, yielding fracture stresses and creep data, respectively. The results reveal a decrease of the strength at operation relevant temperatures for as-joined H–P bar type material due to viscous deformation effects. The almost fully crystallized B bar type material exhibits no measureable strength decrease at elevated temperatures. The head-to-head joined H–P specimens clearly reveal an influence of the sealant layer thickness on the fracture stress which can be associated with a decrease of the compressive residual stress in the layer with increasing thickness. Contrary to this the fracture stresses of material B did not show a dependency on sealant thickness due to its residual stress free state. All H–P and B specimens showed similar fracture behavior with the fracture path being in the layers. The annealed head-to-head joined sealant H–P has a higher strength compared with non-annealed as-joined state and the value remains stable at elevated temperature probably associated with the progressing crystallization.

Steady state creep rates have been obtained. Creep effects are significant around or above T_g as verified for the H–P material. Annealed H–P material displays less creep than the sintered material at any respective temperature, probably related to the increased fraction of crystalline phase inside the material. The associated activation energies for as sintered bars H–P are higher (above 400 kJ mol⁻¹) compared with as sintered bars B and annealed bars H–P indicating a thermally activated crystallization kinetics for sintered bars H–P. It was observed that the stress exponent for the sintered bars H–P increases with temperature, which is considered to be a result of a mechanism change from diffusional to viscous creep, whereas for annealed H–P material and sintered B material it is almost constant ($n \sim 1$). Considering the real application of sealant H–P and B, the fracture behavior of annealed H–P and sintered B appears also to be superior. If the joining procedure can be improved to gain bar like strengths the potential for application of this sealant will be significantly enhanced.

Acknowledgments

The authors would like to express their gratitude to Dr. S. M. Groß who designed, developed and made available the sealant material for the mechanical tests, Mr. D. Federmann for the screen printing of the material and to Dr. D. Grüner for the SEM investigations. The experimental support by Ms. T. Osipova and Mr. J. Mönch is highly appreciated.

References

- [1] S.C. Singhal, K. Kendall, *High Temperature Solid Oxide Fuel Cells*, Elsevier Ltd., Amsterdam, 2003.
- [2] R. Steinberger-Wilckens, L. Blum, H.-P. Buchkremer, L. De Haart, J. Malzbender, M. Pap, *ECS Trans.* 35 (2011) 53.
- [3] S.M. Gross, T. Koppitz, J. Remmel, U. Reisgen, *J. Am. Ceram. Soc.* 26 (2008) 239.
- [4] T. Bause, J. Malzbender, M. Pausch, T. Beck, L. Singheiser, *Fuel Cells*, <http://dx.doi.org/10.1002/fuce.201200181>.
- [5] L. Blum, S.M. Gross, J. Malzbender, U. Pabst, M. Peksen, R. Peters, I.C. Vince, *J. Power Sources* 196 (2011) 7175–7181.
- [6] Y. Zhao, J. Malzbender, S.M. Gross, *J. Eur. Ceram. Soc.* 31 (2011) 541.
- [7] J. Malzbender, Y. Zhao, *Fuel Cells* 12 (2012) 47.
- [8] J. Malzbender, Y. Zhao, *J. Power Sources* 239 (2013) 500–504.
- [9] G. Pečanac, S. Baumann, J. Malzbender, *J. Membr. Sci.* 385–386 (2011) 263–268.
- [10] J. Malzbender, R.W. Steinbrech, *J. Eur. Ceram. Soc.* 28 (2008) 247–252.
- [11] J. Malzbender, R.W. Steinbrech, L. Singheiser, *CESP* 26 (2005) 293–298.
- [12] O. Tokarev, L. Schnetter, T. Beck, J. Malzbender, *J. Eur. Ceram. Soc.* 33 (2013) 749–757.
- [13] W. Araki, D. Hanashiro, Y. Arai, J. Malzbender, *Acta Mater.* 61 (2013) 3082–3089.
- [14] B. Rutkowski, J. Malzbender, T. Beck, R.W. Steinbrech, L. Singheiser, *J. Eur. Ceram. Soc.* 31 (2011) 493–499.
- [15] M. Lipińska-Chwalek, G. Pečanac, J. Malzbender, *J. Eur. Ceram. Soc.* 33 (2013) 1841–1848.
- [16] J. Malzbender, Y. Zhao, *J. Mater. Sci.* 47 (2012) 4342–4347.
- [17] M.W. Barsoum, *Fundamentals of Ceramics*, CRC Press, Boca Raton, 2003.
- [18] G.P. Kothiyal, M. Goswami, B. Tiwari, K. Sharma, A. Ananthanarayanan, L. Montagne, *J. Adv. Ceram.* 1 (2012) 110.
- [19] D. Fátyay, J. Gubicza, J. Lendvai, *J. Alloys Compd.* 434–435 (2007) 75.
- [20] C.Y.S. Chang, W.C.J. Wei, C.H. Hsueh, *J. Non-Cryst. Solids* 357 (2011) 1414.
- [21] B. Kuhn, C.A. Jimenez, L. Niewolak, T. Hüttel, T. Beck, H. Hattendorf, L. Singheiser, W.J. Quadakkers, *J. Mater. Sci. Eng.* 528 (2011) 5888.
- [22] J. Laurencin, G. Delette, F. Usseglio-Viretta, S. Di Iorio, *J. Eur. Ceram. Soc.* 31 (2011) 1741.